



HAL
open science

Paleo-Evolution of Martian Subsurface Ice and Its Role in the Polar Physical and Isotopic Layering

E. Vos, O. Aharonson, N. Schörghofer, F. Forget, L. Lange, E. Millour

► **To cite this version:**

E. Vos, O. Aharonson, N. Schörghofer, F. Forget, L. Lange, et al.. Paleo-Evolution of Martian Subsurface Ice and Its Role in the Polar Physical and Isotopic Layering. *Journal of Geophysical Research. Planets*, 2023, 128, 10.1029/2023JE007822 . insu-04472093

HAL Id: insu-04472093






<https://insu.hal.science/insu-04472093>

Submitted on 22 Feb 2024

HAL is a multi-disciplinary open access archive for the deposit and dissemination of scientific research documents, whether they are published or not. The documents may come from teaching and research institutions in France or abroad, or from public or private research centers.

L'archive ouverte pluridisciplinaire **HAL**, est destinée au dépôt et à la diffusion de documents scientifiques de niveau recherche, publiés ou non, émanant des établissements d'enseignement et de recherche français ou étrangers, des laboratoires publics ou privés.

Paleo-Evolution of Martian Subsurface Ice and Its Role in the Polar Physical and Isotopic Layering

E. Vos¹ , O. Aharonson^{1,2} , N. Schörghofer² , F. Forget³ , L. Lange³ , and E. Millour³

¹Department of Earth & Planetary Sciences, Weizmann Institute of Science, Rehovot, Israel, ²Planetary Science Institute, Tucson, AZ, USA, ³Laboratoire de Météorologie Dynamique/IPSL, Sorbonne Université, ENS, PSL Research University, Ecole Polytechnique, CNRS, Paris, France

Key Points:

- Subsurface-atmosphere vapor (ice) exchange is modeled over Milankovitch cycles using Mars climate and subsurface models
- In regions where subsurface ice periodically forms and disappears due to vapor diffusion, ice concentrations are expected to be small
- The pore-ice volume lost between 5 and 2.5 Myr ago is equivalent to a layer of max-imum thickness 95 m distributed over the North Polar Layered Deposits

Supporting Information:

Supporting Information may be found in the online version of this article.

Correspondence to:

E. Vos,
eran.vos@weizmann.ac.il

Citation:

Vos, E., Aharonson, O., Schörghofer, N., Forget, F., Lange, L., & Millour, E. (2023). Paleo-evolution of Martian subsurface ice and its role in the polar physical and isotopic layering. *Journal of Geophysical Research: Planets*, 128, e2023JE007822. <https://doi.org/10.1029/2023JE007822>

Received 16 MAR 2023

Accepted 18 SEP 2023

Abstract Mars harbors ice deposits in several forms, on the surface and in the subsurface, which exchange with each other on various timescales. We seek to study the pore ice evolution over millennial time scales and how it contributes to and affects the Polar cap's evolution. We calculate the evolution of SubSurface Ice (SSI) pore filling by coupling two models, the Mars LMD Global Climate Model, which calculates the atmospheric and surface evolution on an annual timescale, and the dynamical version of the Mars Subsurface Ice Model, which calculates the evolution of the SSI on a millennial timescale. The SSI latitudinal boundary fluctuates over more than 25° in one obliquity cycle, overall extending equatorward of latitude ±35° at high obliquity, and receding to about ±60° at low obliquity. In locations where the SSI is stable continuously over orbital cycles, the simulations predict layering caused by a sublimation front at the SSI top boundary. Between 5 and 2.5 Myr ago, the subsurface lost at least ~95 m of polar equivalent layer ice. The SSI flux routinely reaches ~1 mm/ Mars year. In addition to the direct contribution to the growth of the North Polar Layered Deposits (NPLD), the SSI causes variations in the NPLD accumulation rate due to the changes in the SSI distribution that affect the seasonal energy budget. These variations are comparable to the change in rate due to variations in orbital elements. When running paleo-climate simulations, particularly to reconstruct the NPLD profile, changes in the SSI distribution should be considered.

Plain Language Summary Ice on Mars is abundant and can be found on the surface and in the subsurface. In this work, we model the evolution of subsurface ice by diffusion. We examine how the evolution of the subsurface affects the North Polar cap stratigraphy. We use humidity calculated by a Global Climate Model and a thermal diffusion model to calculate the growth and retreat of ice in the subsurface. We calculate the depth and the fraction of pore-filling ice at present. The subsurface can contribute ~95 m (of the overall ~2,000 m) of the North Polar Cap column. Subsurface ice indirectly affects the accumulation rate and isotopic ratio of the North Polar Cap growth by changing the seasonal energy budget. This occurs because when ice extends in the subsurface, it changes the thermal properties of the ground. These results emphasize the importance of the subsurface ice in the Martian water cycle, and it needs to be considered when reconstructing the North Polar Cap profile.

1. Introduction

The distribution of SubSurface Ice (SSI) on Mars is essential for the long-term water cycle and for future human exploration. The Phoenix lander removed a few centimeters of regolith to expose stable subsurface ice at latitude 68° (Mellon et al., 2009; Sizemore et al., 2010; Smith et al., 2009), and confirmed previous modeling work that predicted SSI would be stable at the landing site (Mellon & Jakosky, 1993, 1995). Models suggest that the present equilibrium SSI is expected at about ±55° (Diez et al., 2008; Mellon et al., 2004; Schorghofer & Aharonson, 2005). Studies using multiple observational data sets (Morgan et al., 2021), including the Mars Odyssey Neutron Detector (Boynton et al., 2002), the Trace Gas Orbiter Fine-Resolution Epithermal Neutron Detector (Malakhov et al., 2022), fresh craters (Byrne et al., 2009; Dundas et al., 2021, 2023), radar returns (Morgan et al., 2021), seasonal surface temperature variations (Bandfield & Feldman, 2008; Piqueux et al., 2019), and surface geomorphology (Kreslavsky & Head, 2002; Morgan et al., 2021) confirm the presence of SSI, but it extends as far equatorward as 35°N. Previous modeling work showed that the SSI distribution is changing in response to changes in obliquity. In the past, when the obliquity was higher, the SSI extended toward the equator (Jakosky & Carr, 1985; Mellon & Jakosky, 1993, 1995; Schorghofer, 2007, 2010; Schorghofer & Forget, 2012).

Laskar et al. (2004) calculated Mars's orbital elements for the last 21 Myr. During this epoch, the obliquity varied from $\sim 13^\circ$ to $\sim 47^\circ$ and the eccentricity from circular orbit to 0.12. During these cycles, ice can be emplaced in the subsurface in two ways. First, it may be emplaced as a surface layer that subsequently partially sublimates, leaving behind a lag. Alternatively, it may be directly deposited from atmospheric water vapor in the subsurface pores. This mechanism was suggested by Mellon and Jakosky (1993) and verified in the laboratory by Hudson et al. (2009). As ice fills the pores in the subsurface, the bulk thermal inertia increases (Mellon & Jakosky, 1993). For larger subsurface thermal inertia values, more heat is stored in the summer and released in the winter. Hence, changes in the SSI distribution alter the seasonal heat budget. Haberle et al. (2008) showed that this mechanism affects the seasonal CO_2 cycle. Later Vincendon et al. (2010) proposed that this effect also explains the presence of seasonal CO_2 frost on pole-facing slopes at low latitudes.

It has long been understood that changes in atmospheric water vapor content drive changes in subsurface ice volume (Leighton & Murray, 1966; Mellon & Jakosky, 1993, 1995). When the atmosphere becomes drier, subsurface ice is lost to the atmosphere. When the atmosphere becomes more humid, empty pore spaces gradually fill with ice due to vapor diffusion and desublimation. The extent of the latitudinal variation of SSI due to variations in orbital elements has previously been explored either with microphysical models of vapor diffusion (Mellon & Jakosky, 1993; Schorghofer & Aharonson, 2005) or with models of the equilibrium ice table (Mellon & Jakosky, 1995). The equilibrium ice table represents the depth-to-ice where an equilibrium is reached between the atmospheric vapor content and the saturation vapor pressure at the ice. These models established that the equatorward boundary of the SSI is expected to oscillate by tens of degrees over obliquity cycles (e.g., Aharonson et al., 2022; Mellon & Jakosky, 1995). A change of 1° in latitude of the subsurface ice layer margins corresponds to an area of $6 \times 10^5 \text{ km}^2$ at latitude 60° , comparable to the size of the North Polar Cap. And the margin has moved by far more than 1° . Hence, changes in SSI volume can potentially be a major contribution to the global water ice cycles, including the history of the Polar Layered Deposits. To calculate changes in SSI volume due to orbital variations neither microphysical diffusion models nor equilibrium ice table models suffice. Microphysical models are computationally too slow and equilibrium ice table models only describe the solution after an asymptotically long time, whereas at latitudes where SSI repeatedly appears and disappears, there is not enough time to reach this asymptotic solution. Long-term changes in ice volume can be calculated with a more complex model described in Schorghofer (2010). It is here referred to as the “dynamical Mars Subsurface Ice Model (MSIM),” to distinguish it from the “static” computations of an equilibrium ice table, which are also part of the MSIM collection. Calculations with GCM-based atmospheric humidities and zonally averaged SSI were published in Schorghofer (2007) and Schorghofer and Forget (2012) and suggest that the SSI margin moved between about 30° and 65° over the last 3 Myr. Here these model calculations are extended using (a) updated and more detailed GCM-based atmospheric vapor content maps, (b) extension to longitude-dependent rather than zonally averaged maps, and (c) inclusion of the modulations induced by ground ice variations on the PLD long-term growth sourced from an equatorial reservoir.

The accumulation rate of the North Polar Layered Deposits (NPLD) is a function of the orbital elements and the surface ice distribution (Emmett et al., 2020; Levrard et al., 2007; Vos et al., 2022a, 2022b). Vos et al. (2019), using a box model, argued that an isotopic signal should be present in the NPLD stratigraphy that records the orbital cycles. This was later supported by detailed GCM simulations that showed that the isotopic layering is controlled by the orbital elements and the surface ice distribution (Vos et al., 2022a, 2022b).

Our objectives here are three-fold: First, to quantify the evolution of the pore-filling subsurface ice over orbital cycles on a millennial timescale. Second, to quantify the contribution of the SSI to the NPLD growth. And third, to evaluate the indirect effects of the SSI on the physical and chemical evolution of the PLD.

We begin by following Schorghofer and Forget (2012) and calculate the evolution of the SSI at high resolution using MSIM (Schorghofer, 2010), with more accurate boundary conditions. The humidity at each latitude is retrieved from the Mars Planetary Climate Model (PCM) (Forget et al., 1999) for present-day ice distribution and various orbital combinations (Table 1). We then evaluate the vapor flux from the subsurface and its significance as a source for NPLD growth. Lastly, we test the effect of different SSI distributions on the NPLD accumulation rate and isotopic ratio by running the Mars PCM with different subsurface thermal inertia values corresponding to different SSI distributions (Table 2).

Table 1
Summary of the Orbital Configurations for Which GCM Simulations Were Performed

Obliquity	$e = 0$	$e = 0.045$	$e = 0.093$	$e = 0.125$
10°	0°	0°, 90°, 270°	0°, 90°, 270°	0°, 90°, 270°
15°	0°	0°, 90°, 180°, 270°	0°, 90°, 180°, 270°	0°, 90°, 180°, 270°
20°	0°	0°, 90°, 180°, 270°	0°, 90°, 180°, 270°	0°, 90°, 180°, 270°
25°	0°	0°, 90°, 180°, 270°	0°, 45°, 90°, 135°, ...315°	0°, 90°, 180°, 270°
30°	0°	0°, 90°, 180°, 270°	0°, 90°, 180°, 270°	0°, 90°, 180°, 270°
35°	0°	0°, 90°, 270°	0°, 45°, 90°, 135°, ...315°	0°, 90°, 270°
40°	0°	90°, 270°	0°, 90°, 270°	90°, 270°
45°	0°	90°, 270°	0°, 90°, 270°	90°, 270°
50°	0°	0°, 90°, 270°	0°, 90°, 270°	0°, 90°, 270°

Note. The entries in the table list the L_p values used for each eccentricity and obliquity combination. At $e = 0$ the value of L_p is arbitrary.

2. Model Description

In this work, we use two models; the first is the Mars PCM (previously known as the LMD Mars GCM) (Forget et al., 1999) to calculate the annual mean atmospheric humidity and the physical and isotopic evolution of the NPLD. The second is a component of MSIM (Schorghofer, 2010), a collection of programs focused on 1D growth and retreat of SSI on Mars.

The Mars PCM used here has the complete water cycle that includes treatment of surface ice, atmospheric vapor, HDO tracer, and ice clouds and has been described in detail previously (Forget et al., 1999; Madeleine et al., 2009, 2011; Montmessin et al., 2004; Rossi et al., 2021). The model simulates the Martian atmospheric processes such as turbulence mixing, cloud condensation, ice sedimentation, gravity waves, HDO isotopic fractionation, as described in the cited papers. In addition, it simulates surface-atmosphere interactions such as CO₂ and water sublimation. We use the PCM to calculate the atmospheric humidity with a time step of a few minutes. Then we calculate the annual mean humidity at each grid cell for different orbital configurations (Table S1 in Supporting Information S1). The GCM resolution (64 longitudes × 65 latitudes × 29 vertical layers) and the choice of parameters are identical to that published in Vos et al. (2022a, 2022b) except for Section 3.2, where we modified the subsurface thermal inertia according to the distribution of SSI similar to results computed in MSIM and added a tropical ice source. We elaborate on these changes in the Results section. For the zonal MSIM simulations, we interpolate the humidity retrieved from the PCM to a 1° resolution. We performed 106 PCM simulations

(Table S1 in Supporting Information S1), covering the range of orbital combinations that have occurred in the last 21 Myr (Laskar et al., 2004). We calculated each simulation's annual mean humidity at each grid cell. We linearly interpolate among the orbital parameters data points for the humidity. Figure S2 in Supporting Information S1 shows the annual mean humidity simulations points (crosses) and the interpolation for two slices through the hyper-dimensional parameter space: humidity as a function of obliquity and latitude for a circular orbit, and humidity as a function of obliquity and longitude of perihelion (L_p) at latitude 45° for present-day eccentricity of 0.093. The radiative effects of water ice clouds are neglected. This effect can alter the atmospheric and surface temperature by several degrees for larger obliquities than present (Madeleine et al., 2014), when the atmospheric humidity was higher, leading to a model inaccuracy in our calculations. Latent heat fluxes in the surface water phase changes are negligible for the sublimation/accumulation rates we find and are not taken into account. Some parameters in the PCM are assumed to be like at present, such as bare ground albedo, atmospheric dust loading, and surface thermal inertia. These parameters can

Table 2
Best-Fit Coefficients and Their Error Estimates for the Function $h(i_{ss}, \phi)$, as Defined in Equation 4

Coefficient	Value	Error	Units
$h_0^{(0)}$	0.30	1.37×10^{-4}	Pa
$h_1^{(0)}$	3.41×10^{-6}	6.37×10^{-7}	Pa
$h_1^{(1)}$	0.056	0.0086	W ⁻¹ m ²
$h_1^{(2)}$	-4.96×10^{-5}	1.07×10^{-5}	W ⁻² m ⁴
ϕ_0	84.85	0.042	°
$\phi_\sigma^{(0)}$	18.35	0.85	°
$\phi_\sigma^{(1)}$	-2.21×10^{-3}	1.02×10^{-4}	W ⁻¹ m ²
β_1	2.00×10^{-2}	1.4×10^{-3}	W ⁻¹ m ²
β_2	7.42×10^{-3}	2.83×10^{-4}	W ⁻¹ m ²

change with the planet's evolution but have a secondary effect on the humidity compared to the orbital configuration (Madeleine et al., 2009).

MSIM is a collection of programs that includes 1D models for microphysical subsurface vapor diffusion and accumulation, the equilibrium ice table, and a computationally fast model for long-term SSI volume changes. The last of these three types of models is used in this work. The full description of the model and the equations can be found in Schorghofer (2010). MSIM assumes flat ground and uses as input the elevation calculated from MOLA data (Smith et al., 2001), the surface thermal inertia and albedo values from TES (Putzig et al., 2005), the computed past orbital parameters (Laskar et al., 2004), and the humidity as described above. The model calculates temperatures in 30 min intervals over several Mars years, until temperatures have equilibrated. Temperatures from the last Mars year are used to calculate and then time-average sublimation rates at every vertical grid point, hence incorporating the role of diurnal and seasonal temperature amplitudes. This information is then used to evolve the pore ice volume over 1 Kyr, using theoretical formulas for the rate of growth or depletion. The thermal properties depend on the ice content and are periodically updated. This asynchronous coupling between a thermal model with a small time step and an ice volume evolution model with a large time step makes it possible to integrate over millions of years. At each 1 Kyr time step, we update the orbital configuration and the humidity at each grid cell and calculate the SSI evolution. Porosity is defined as the void volume fraction over the total volume and is assumed to be 0.4. We use a value of $4 \times 10^{-4} \text{ m}^2 \text{ s}^{-1}$ for the free-gas diffusion coefficient at 600 Pa, and it can change as a function of surface pressure and as ice fills the pores (Schorghofer, 2010). Kinetics of phase transition are averaged out, and the temporal dependence that arises from diffusion and heat propagation in the subsurface are included in the model (Schorghofer, 2010). We initialized the model 10 Myr ago with pores empty of ice. We tested the model with a geothermal heat flux of 0.028 W m^{-2} and no geothermal heat flux. The two cases showed similar SSI latitudinal evolution, with small differences in ice table depth, and growth rate. Figure S5 in Supporting Information S1 shows the pore-filling evolution as a function of time and depth for both cases. Hence, we choose to neglect the geothermal heat flux in this work. The spatial resolution in the MSIM zonal runs is 1° in latitude, and for geographically resolved runs it is 4.37° in longitude and 2.185° in latitude. There are 80 log-spaced vertical layers down to a depth of 8 m in all simulations; we also tested with a 16 m maximum domain, and the results were similar.

To simplify the modeling, an assumption is made: subsurface ice is assumed to reside in pore spaces rather than in the form of massive ice. There is abundant evidence of glaciations on Mars that resulted in massive ice sheets and buried massive ice, but the timing and volume of these glaciations are highly uncertain. Hence, our model results are applicable only to the period since the last glaciation. Put differently, the calculated subsurface pore-ice volume changes represent a maximum, since massive ice sheets compete with the availability of regolith pore space. Regolith adsorption is not taken into account in this work, but is not expected to have a significant impact over orbital timescales (Schorghofer & Aharonson, 2005).

3. Results

The result section is divided into two parts. The first summarizes the evolution of the SSI pore ice in the last several Myr. The second part calculates the dependence of the NPLD accumulation rate and isotopic ratio on the SSI distribution when surface tropical ice is present.

3.1. Subsurface Ice Evolution

The SSI's growth and retreat are controlled by the atmospheric humidity and the subsurface temperature profile (Mellon & Jakosky, 1993; Schorghofer & Aharonson, 2005). We run GCM simulations (Table S1 in Supporting Information S1) and calculate the humidity at various past orbital conditions. We apply an elevation correction when averaging the humidity as follows. Assuming a constant water mixing ratio near the surface, we correct the surface partial pressure of water to the zonal mean elevation and then compute the zonal mean humidity. The zonal annual mean altitude-corrected humidity is shown in Figure 1 in μm as a function of time and latitude. The top figure show interpolated data (for the data points from Table 1 and the interpolation, see Figures S1 and S2 in Supporting Information S1) using different orbital configurations for every 1 Kyr (Laskar et al., 2004). When the obliquity value is larger, more ice sublimates from the NPLD during summer. Hence, more water vapor is in the north pole region down to latitude 50° , and moisture is transported to lower latitudes and the southern hemisphere. This phenomenon is amplified when the summer

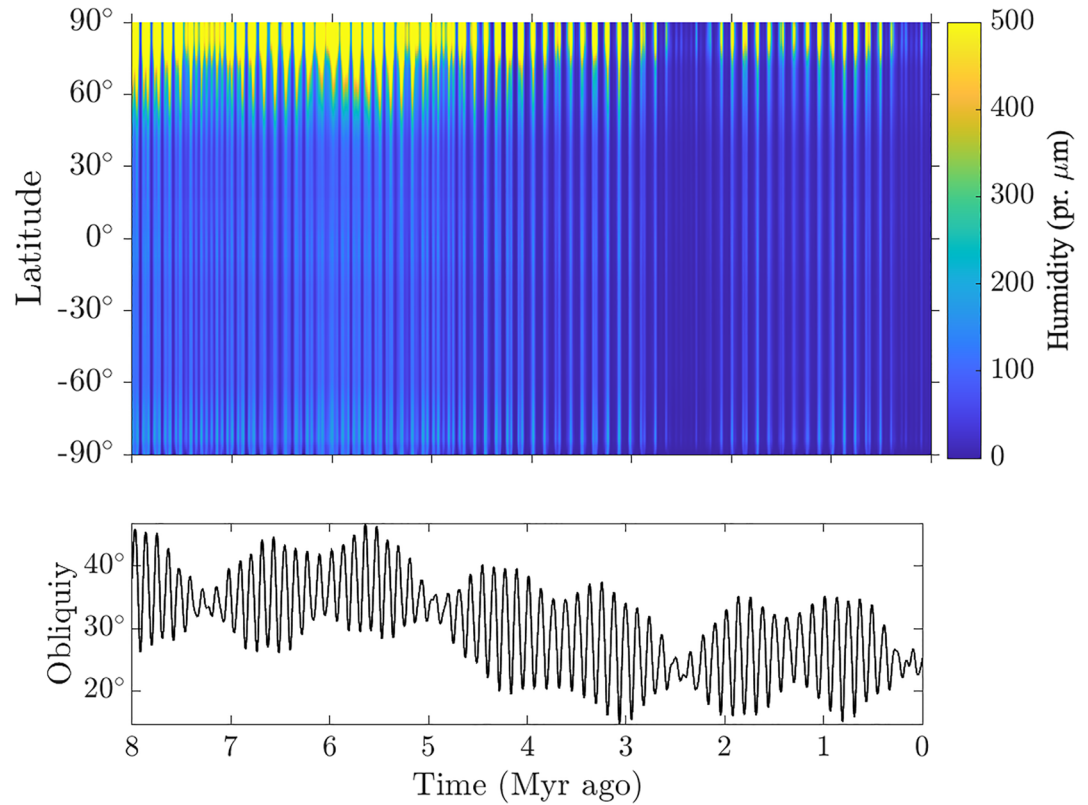


Figure 1. Top panel: zonal annual mean humidity in μm as a function of latitude and time. Bottom panel: Obliquity as a function of time (Laskar et al., 2004).

is more extreme in the northern hemisphere ($L_p = 90^\circ$). At present-day orbital configuration, the atmosphere is relatively dry because when the northern summer is long and mild ($L_p = 251^\circ$), the amount of ice that sublimates from the NPLD is dramatically lower than when the northern hemisphere summer is short and intense (Levrard et al., 2007).

Our simulation results allow deriving an analytic approximation for the dependence of the annual mean humidity on the orbital configuration. Following Levrard et al. (2007), we parameterize this relation as a function of the corrected insolation at the summer solstice (i_{ss}), given by

$$i_{ss} = S_0 \sin \epsilon \frac{1 + e \sin L_p}{1 - e^2} \sqrt{\frac{1 - e^2}{1 + e^2 + 2e \sin L_p}}, \quad (1)$$

where $S_0 = 589.2 \text{ W m}^{-2}$ is the solar constant at Mars, ϵ is obliquity, and e is eccentricity and L_p is the perihelion alignment. The form of the approximation for the global annual mean humidity h we find is an exponential function of i_{ss} given by

$$h(i_{ss}) = 0.4 e^{\alpha(i_{ss} - i_{ss0})}, \quad (2)$$

where h has units of Pascal, $i_{ss0} = 350 \text{ W m}^{-2}$, and α is given by

$$\alpha = \begin{cases} 0.0205 & i_{ss} \leq i_{ss0} \\ 0.0075 & i_{ss} > i_{ss0}. \end{cases} \quad (3)$$

The humidity results from the simulation, along with this fit, are shown in Figure 2. This parameterization improves upon previous humidity approximations as a function of obliquity only (Mellon & Jakosky, 1995;

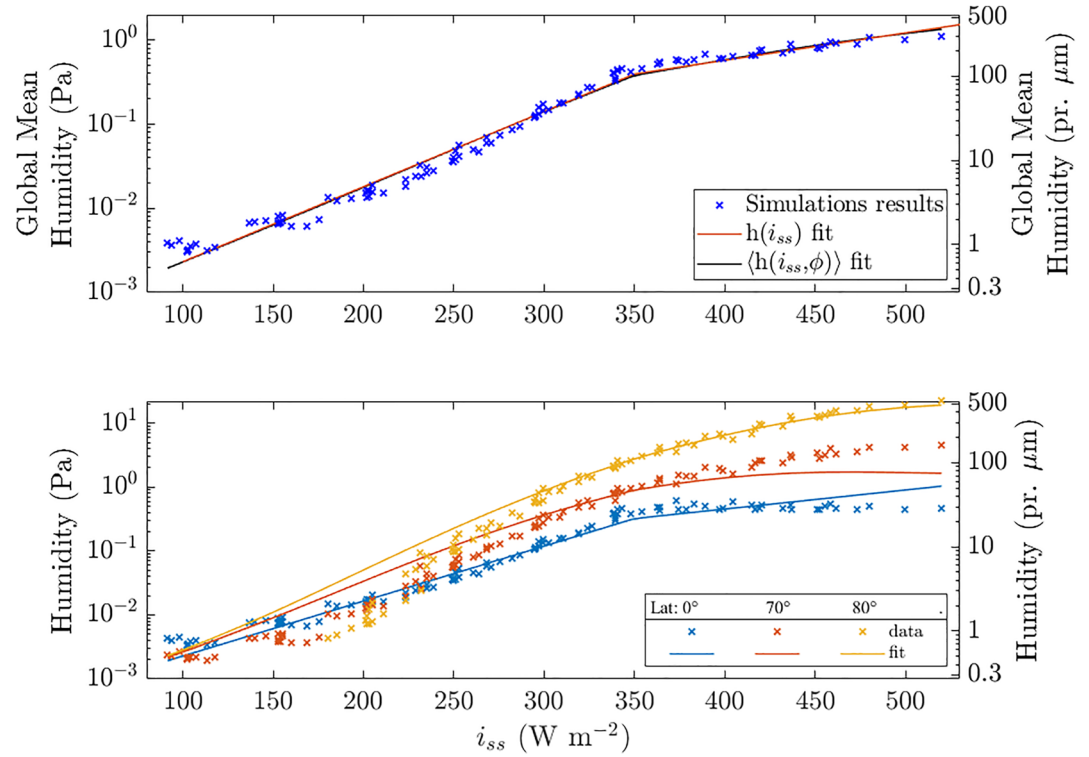


Figure 2. Top: Global annual mean humidity as a function of i_{ss} , blue crosses are GCM simulations results, the red line is the fit to the globally averaged humidity given by Equation 4, the black line is the global mean of the latitude-dependent fit given by Equation 6. Bottom: Humidity results and fits for select latitudes calculated from Equation 6.

Mellon & Sizemore, 2022; Schorghofer & Forget, 2012), by including the effect of eccentricity and L_p , using the i_{ss} dependence, which collapses the data nicely onto a broken exponential function.

The global mean value of humidity does not capture the strong latitude dependence of h (Figure S4 in Supporting Information S1). Thus, we extend the parameterization using a shifted Gaussian function of latitude, truncated at the pole. We employ a multi-parameter fit to describe the combined latitudinal and insolation dependence. The combined parameterization for the humidity function is then

$$h(i_{ss}, \phi) = h_1(i_{ss}) \exp\left(\frac{(\phi - \phi_0)^2}{2\phi_\sigma^2(i_{ss})}\right) + h_0(i_{ss}), \quad (4)$$

where h_0 , h_1 , and ϕ_σ are parameterized functions of i_{ss} , and ϕ_0 is the fit parameter indicating the latitude of maximum humidity. The parameterizations and best-fit coefficients are:

$$h_0 = 0.3 \exp(\beta (i_{ss} - i_{ss0})), \quad (5)$$

$$h_1 = 3.41 \times 10^{-6} \exp(-4.96 \times 10^{-5} i_{ss}^2 + 0.0563 i_{ss}), \quad (6)$$

$$\phi_0 = 84.85^\circ \quad (7)$$

$$\phi_\sigma = 18.35^\circ \exp(-0.0025 i_{ss}) \quad (8)$$

where β is given by

$$\beta = \begin{cases} 2 \times 10^{-2} & i_{ss} \leq i_{ss0} \\ 7.42 \times 10^{-3} & i_{ss} > i_{ss0}. \end{cases} \quad (9)$$

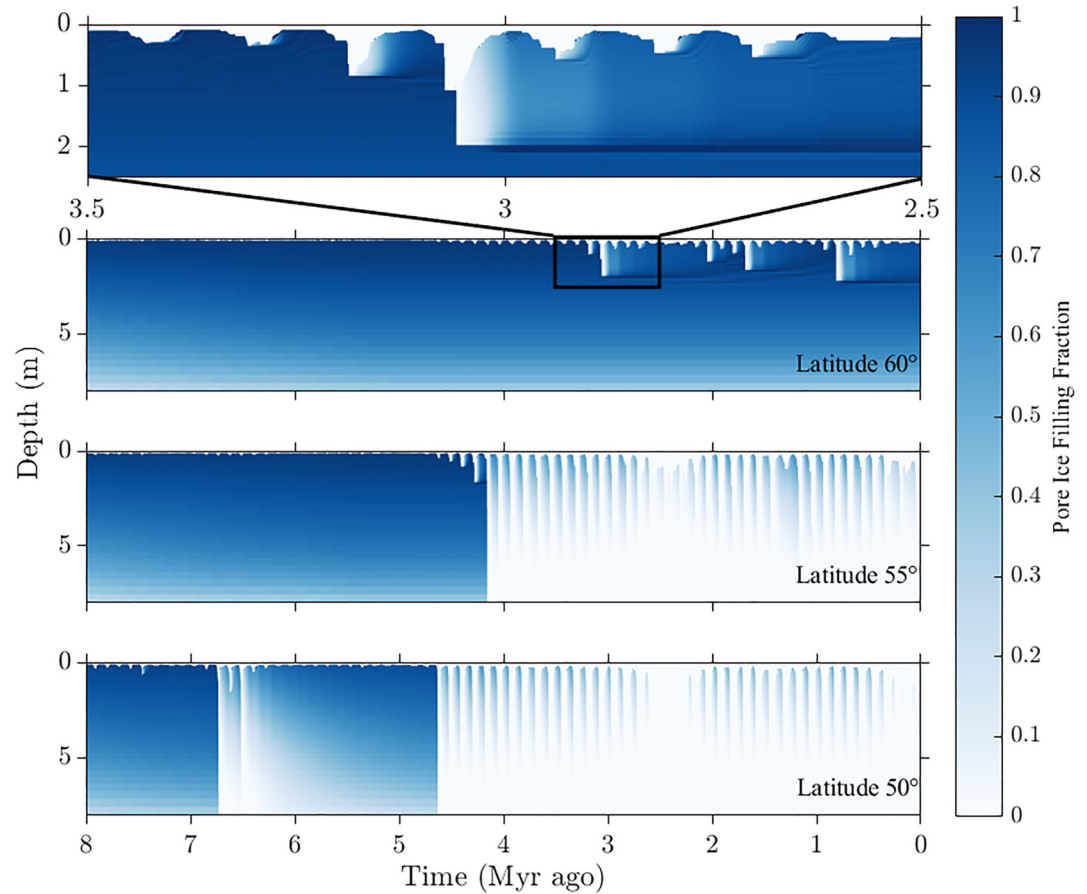


Figure 3. SSI evolution at latitudes 60°N, 55°N, and 50°N. An interesting feature emerges when the SSI experiences an abrupt increase in the stability depth. For example, just before 3 Myr ago at latitude 60°(top panel), the ice table retreats to ~2 m depth over several Kyr. In subsequent time the orbital configuration allows the SSI to refill the empty pores above ~2 m depth, but a record of the ice-table retreat event appears in the form of a layer of increased ice density which persists for long timescales. At 55°N, the transition 4.5 Myr ago from continuously to periodically stable ice is evident. At 50°N, a diffusion-limited ice-table periodically develops for several 100s of Kyr.

and i_{ss0} is the same as before. The coefficients as a function of i_{ss} are shown Figure S3 in Supporting Information S1, and their error estimates are provided in Table S2 in Supporting Information S1. The humidity h_x has units of Pascal, and ϕ_x is in degrees. The combined fit to the simulations results is shown in Figure 2. The bottom panel shows the fit at several select latitudes. The top panel also shows the global mean of the latitude-dependent approximation $\langle h(i_{ss}, \phi) \rangle$, which matches the simulations' results nicely and closely follows the fit to the global mean humidity $h(i_{ss})$.

Both the global mean and latitude-dependant analyses show the simulation results are well-fit with a break in the exponent at $i_{ss0} = 350 \text{ W m}^{-2}$. The origin of this break is not fully understood, but we hypothesize it may be related to saturation of the atmospheric vapor content or a limitation on the vapor transport from the pole to lower latitudes.

We use the annual mean humidity shown in Figure 1 as an input to MSIM and calculate the growth/retreat of ice as a function of time and latitude. Results for the evolution of the SSI for latitudes 60°, 55°, and 50°N are shown in Figure 3. Both the depth of the ice table and the depth-dependent pore-filling fraction change with time. Earlier than 4.5 Myr ago, the obliquity was overall higher (Laskar et al., 2004), the atmosphere was more humid (Figure 1) and the mid-latitude SSI was more stable than during the last 4.5 Myr. Approximately 4.5 Myr ago, the mean obliquity dropped from about 35° to 25° (Laskar et al., 2004), the climate became drier and more insolation reached lower latitudes, and hence, the SSI became less stable in the mid-latitudes. At high latitudes, where the SSI is stable for 100s of Kyr, the depth of the ice table is several centimeters, and it varies only slightly due to

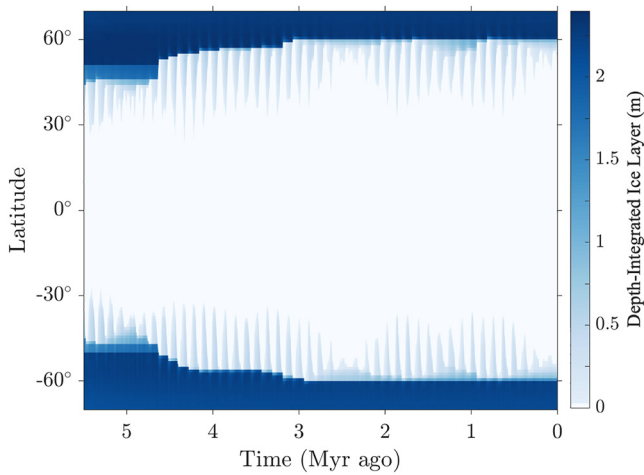


Figure 4. Depth-integrated SSI layer as a function of latitude and time. The bottom of the color scale is discontinuous, with white representing completely empty pores. The SSI extends equatorward when obliquity increases and when atmospheric humidity is higher. In an obliquity cycle, the SSI margin migrates over a range of $\sim 25^\circ$, while over a precession cycle, it migrates over $\sim 10^\circ$.

changes in the humidity and the orbital configuration. Closer to the margin between the SSI and the dry regolith at lower latitudes, the depth to the ice table increases rapidly over a few degrees of latitude to more than a meter and is substantially affected by changes in humidity and orbital configuration. The pore-filling rate at the upper few meters (up to ~ 4 m) is higher than near the bottom of the domain, and the ice fraction shows large variations that mirror the obliquity cycles. We note the effect of variations in obliquity on the SSI in the last 4.5 Myr, except at times when the obliquity is almost constant, from 2.7 to 2.2 Myr ago and from 0.4 Myr ago to the present. At these times, smaller variations in the SSI due to changes in L_p are seen. In general, the growth of the SSI is slow and continuous, while the retreat is rapid because the latter is limited only by diffusion. In contrast, growth is limited by both diffusion and the ability to pump water vapor downward into the subsurface (Schorghofer, 2010).

An interesting feature emerges when the SSI experiences an abrupt increase in the stability depth (Schorghofer, 2009). For example, just before 3 Myr ago at latitude 60° (Figure 3 top panel), the SSI stability depth increases substantially over several Kyr. In subsequent time the orbital configuration allows the SSI to refill the empty pores above ~ 2 m depth, but a record of the ice-table retreat event appears in the form of a layer of increased ice density which persists for long timescales (>1 Myr). We predict that such layering in the SSI can persist and be observable in the high latitudes, and if found, would be a signature of past events of rapid retreat in the ice table.

We track the SSI distribution as in Figure 3 and calculate the depth-integrated SSI volume as a function of latitude shown in Figure 4. Because we chose the depth of the domain to be 8 m, and the assumed porosity is 0.4, the maximum integrated ice layer thickness is 3.2 m of ice. Before 4.5 Myr ago, when the obliquity value was higher (Laskar et al., 2004), SSI extended farther toward the equator. About 4.5 Myr ago, the obliquity dropped from a mean of $\sim 35^\circ$ to a mean of $\sim 25^\circ$. In response to this change, the SSI retreated poleward by about 15° over ~ 2 Myr. There are also variations within the obliquity cycle of $\sim 25^\circ$, and more minor oscillations in L_p when the obliquity is approximately constant, as in the last 400 Kyr. The SSI is continuously stable poleward of latitude $\pm 60^\circ$. In the extreme, when the orbital configuration favors equatorward extension of the SSI, the margin reaches 25° and -27° , respectively. In the last 4.5 Myr, with only rare excursions, the stable ice margin resides between 40° and 60° latitude in both hemispheres. Present-day Mars is relatively dry, so the SSI margin is at the higher end of this range compared to past conditions.

The extent to which subsurface ice is a significant source of water vapor is an important question for understanding the NPLD growth. Having calculated the evolution of the SSI, we examine its bulk changes that represent its exchangeable volume. In the top panel of Figure 5, we plot this quantity integrated between latitude -80° and 80° (excluding the polar regions). Recall, we assume a porosity of 0.4 up to a depth of 8 m. Fluctuations of the SSI occur at the expense of the polar cap and other surface reservoirs. The maximum in the SSI integrated volume over the last 5.5 Myr reaches plus 98 m Polar Equivalent Layer (PEL) defined as a layer evenly spread on the NPLD ($1,040,000 \text{ km}^2$ (Zuber et al., 1998)) at periods of high obliquity and minus 9 m PEL at low obliquity compared to today, the amount of ice lost from the SSI between 5 and 2.5 Myr ago is about 95 m PEL, and the typical SSI flux is <1 mm/yr PEL, rarely reaching a loss rate of 2 mm/yr PEL. These values are of the same order of magnitude as previous estimates of the NPLD accumulation rate when a tropical source is available (Laskar et al., 2002; Milkovich & Head, 2005; Vos et al., 2022a, 2022b). However note, that while the instantaneous fluxes of ice from the SSI and equatorial surface reservoirs may be comparable, over the Myrs time scale of the NPLD growth, the SSI can only contribute ~ 95 m PEL, far from the $\sim 2,000$ m current height of the NPLD. The balance of the net PLD accumulation must be sourced from reservoirs such as surface or buried glaciers, as opposed to the pore-filling subsurface ice in diffusive contact with the atmosphere.

The SSI flux is the time derivative of the SSI integrated volume. The lower panel of Figure 5 shows the power spectrum of the flux for two time windows: 2–1.5 Myr ago, during which the dominant frequency is 120 Kyr, corresponding to the obliquity cycle, and for the time window between 0.5 Myr ago to the present, during which the dominant frequency is 50 Kyr. The latter corresponds to the effect of the precession cycle, with an amplitude

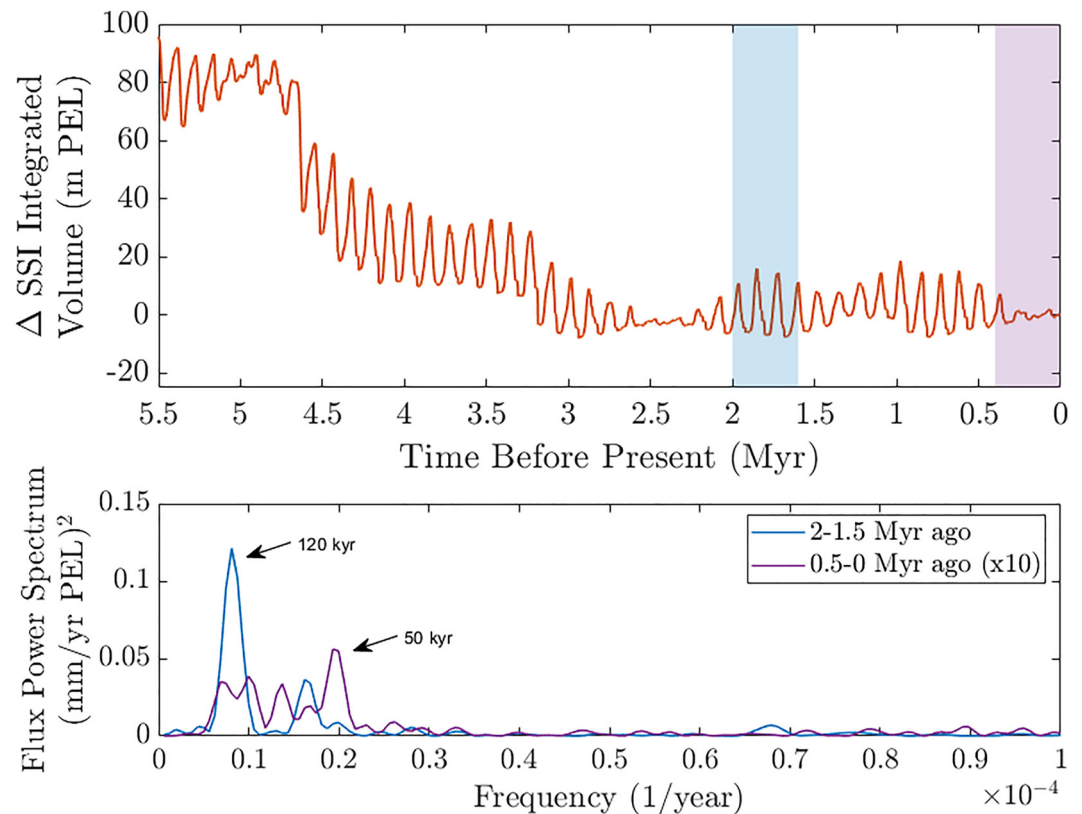


Figure 5. Top: Difference in the SSI integrated volume as a function of time, compared to today (normalized to zero). Overall the amount of ice lost from the SSI between 5 and 2.5 Myr ago is about 95 m Polar Equivalent Layer (PEL), with a typical SSI flux is <1 mm/yr PEL. Bottom: Power spectrum of the flux for present-day surface ice distribution for two selected time windows, 2–1.5 Myr ago and 0.5 Myr ago-present (multiplied by 10), respectively. From 2 to 1.5 Myr ago, the 120 Kyr obliquity signal is dominant, and for 0.5 Myr-present, the weaker precession signal is now dominant.

lower in an order of magnitude than the earlier window, which now emerges in the absence of obliquity variations. The dominance of the precession cycle at latitudes near the ground-ice boundary (near 60°) can be understood in terms of temperature variations, as the influence of obliquity happens to be small at this latitude (Schorghofer, 2008). This precession dependence is shown here to apply even to the latitude-integrated SSI volume.

In addition to the zonal mean fields we present, we also perform MSIM simulations at a lower spatial resolution but including the longitudinal dependency that inherits from the longitudinal differences in topography (Smith et al., 2001), thermal inertia (Putzig et al., 2005), and humidity. The initial conditions for these simulations are the same as those of the zonal mean runs, that is, runs begin 10 Myr ago with empty pores. As before, the model is iterated at 1 Kyr timesteps, now using the full humidity fields obtained from the GCM, still interpolated according to the changing orbital parameters (Laskar et al., 2004).

The present-day depth to the SSI table and the depth-integrated ice layer size are shown in Figure 6. The geographic pattern of the depth variations is in good agreement with neutron observations (e.g., Boynton et al., 2002; Feldman et al., 2002; Mellon et al., 2004), although the neutron-derived maps exhibit more variation with geographic longitude than maps based on SSI models (Schorghofer & Aharonson, 2005). The SSI depth and its integrated thickness show modest departures from zonal symmetry, responding to the longitudinal differences in surface thermal properties, topography, and atmospheric humidity. The filling profile follows two regimes of behavior. Polewards of latitude $\sim 60^\circ$ the SSI is stable continuously, the filling fraction is high and the depth to the ice table is a few cm's. Equatorward of this latitude, the ice-table recedes rapidly over $\sim 10^\circ$ of latitude to several meters in depth and then disappears entirely. Today, the range of latitudes where SSI has been periodically

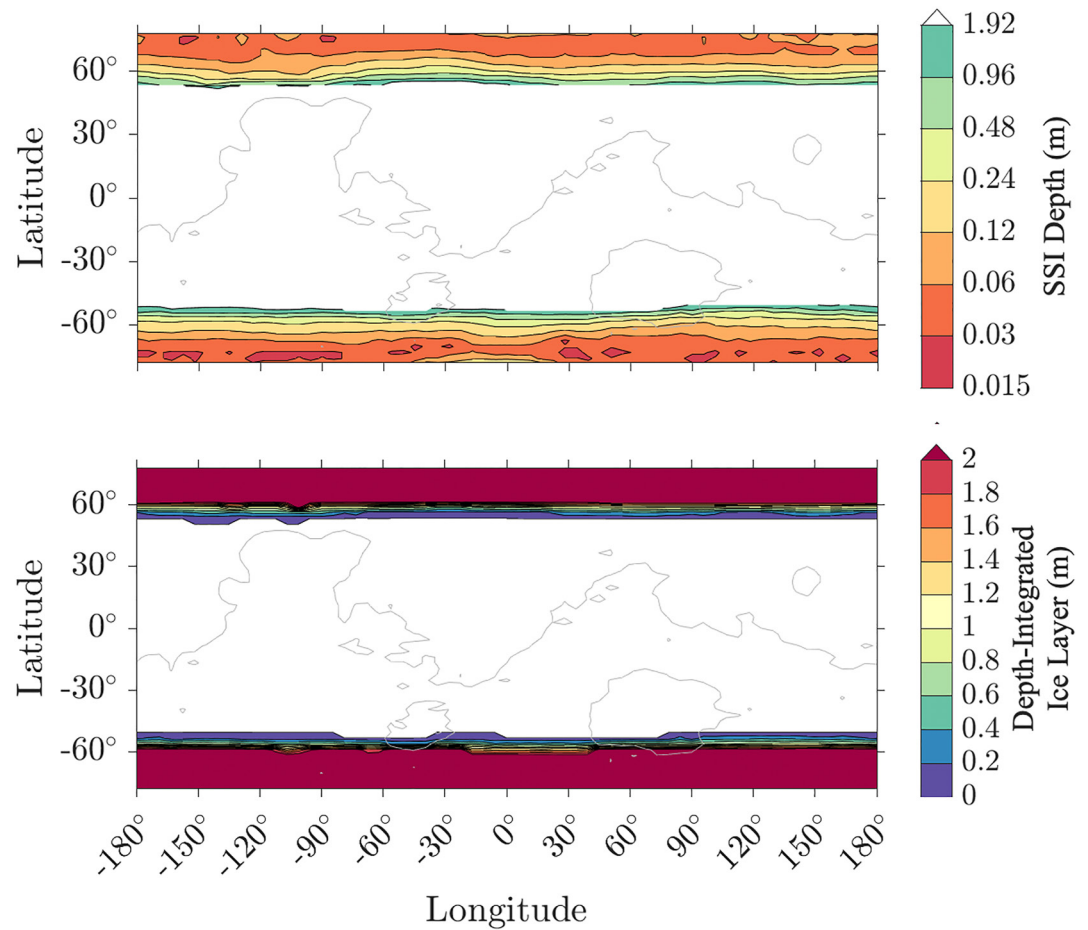


Figure 6. Geographic maps of the depth to SSI (top) and the SSI depth-integrated ice layer thickness (bottom). White represents no stable SSI. The gray contour indicates zero elevation. Some longitude variations are evident in the SSI depth and in the SSI depth-integrated ice layer.

forming is roughly 50–60° expected pore-filling fractions are on the order of 10%, and column-integrated ice volumes are the equivalent of decimeters of pure ice.

In the past, when the atmospheric water content was larger and the SSI extended further, variations in longitude were more significant than today. For example, the SSI depth and the depth-integrated ice layer thickness 863 Kyr ago are shown in Figure 7. This is the most recent time at which obliquity exceeded 35°, and during which the eccentricity was 0.06, and L_p of 143°. The departure from zonal symmetry occurs mostly in the northern hemisphere near the Phoenix landing site in Arcadia Planitia (longitude 150–120°) and near Utopia Planitia (longitude 30–60°). In addition, small concentrations of SSI can also be found in Tharsis and Elysium Mons at this high obliquity. We emphasize that this near-tropical ice is expected to have completely disappeared by now.

3.2. The SSI Thermal Inertia Effect on the NPLD

In the previous section, we calculated the SSI evolution and calculated the integrated ice volume (only pore filling) the SSI can contribute to the NPLD growth. In this section, we calculate the indirect effect of the SSI distribution on the NPLD evolution by running a series of independent PCM simulations with different SSI static distributions and orbital configurations with a tropical ice source. When ice is present in the subsurface, the conductivity, and hence the thermal inertia, increases significantly (Mellon & Jakosky, 1993), altering the seasonal energy budget. We test how different SSI distributions affect (by changing the subsurface thermal inertia) the NPLD accumulation rate and isotopic ratio when a tropical source is present. This is important because The accumulation rate variations are expected to be ultimately responsible for the layer thickness variations in

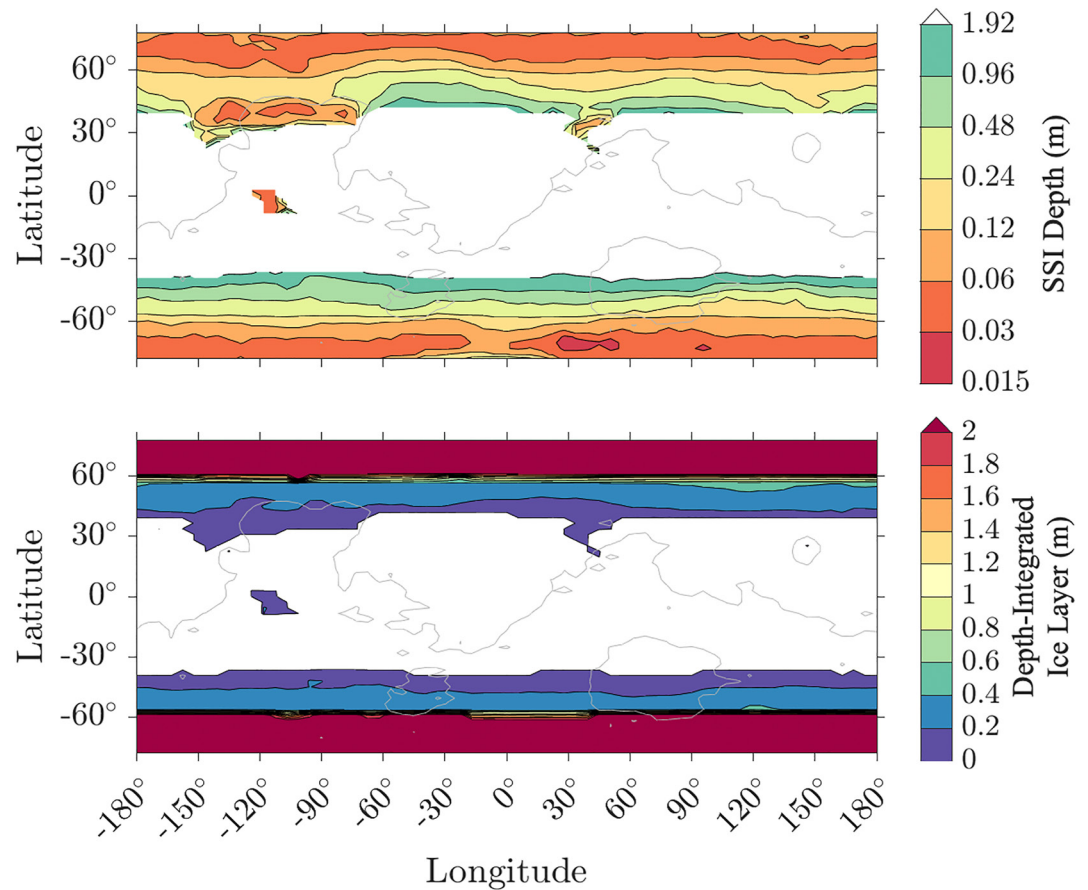


Figure 7. Same as Figure 6 but for 863 Kyr ago. At this time Mars had an obliquity of 35°, eccentricity of 0.06, and L_p of 143°. A significant departure from zonal symmetry is evident.

the observed stratigraphy. We added a surface ice source on the eastern flanks of Tharsis rise (with an area of $\sim 10^6$ km²) where accumulation is predicted at high obliquity (Forget et al., 2006), to allow secular polar growth and ran a series of independent simulations for an extensive range of orbital configurations with several different assumptions on the subsurface thermal inertia that correspond to different SSI distributions. For simplicity, we assumed a uniform layer of a given thermal inertia value, extending from the poles to different latitudes and depths. We performed simulation with $I = 1,200$ tui (SI thermal inertia units, J m⁻² K⁻¹ s^{-1/2}) and $I = 2,000$ tui, the minimum latitudes of the layer of 30° and 60°, and depths of 5, 10, and 15 cm. These are compared to simulations with the thermal inertia distribution obtained from the present reference SSI distribution. When the thermal inertia in the mid-latitudes is higher, the amount of heat conducted to the subsurface and stored during the summer is larger. This heat is released during winter, reducing the summer-winter temperature difference. Figure 8 shows the NPLD ice accumulation rate as a function of L_p (top), obliquity (middle), and eccentricity (bottom), and for different SSI distributions for the near-present orbit. We indicate the comparison case consisting of the reference present GCM subsurface thermal inertia and a nominal orbital configuration with an obliquity of 25°, L_p of 270°, and eccentricity of 0.093 (similar to the present day). In each panel, we modify a different orbital parameter and keep the rest constant, to test the dependence of the NPLD growth rate on each variable. Vos et al. (2022a, 2022b) showed that the growth rate of the NPLD at obliquities of 15–30° is controlled by the intensity of the summer, where a warmer summer allows more vapor to reach the pole. In Figure 8, we can see that in addition to this dependence on orbital geometry, the different SSI distributions have an effect similar in magnitude on the polar accumulation. These results highlight the importance of the SSI distribution in the growth of the PLDs and should be taken into account in models reconstructing its stratigraphy.

In addition to the NPLD growth rate, we also quantify the effect of the SSI distributions on the isotopic ratio of the accumulated ice (Figure 9). At each time step and grid cell, the PCM calculates the temperature-dependent

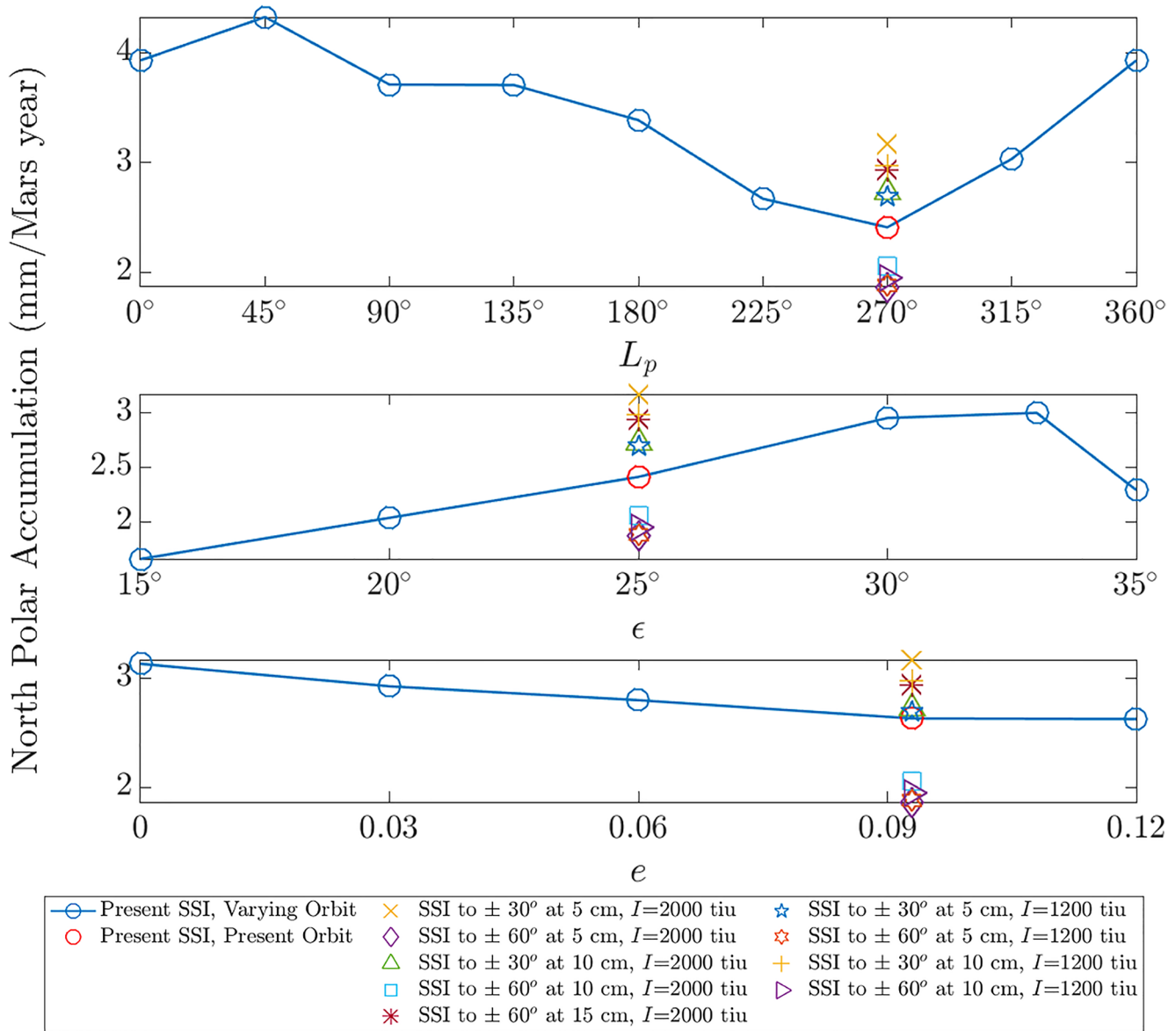


Figure 8. North Polar Layered Deposits (NPLD) ice accumulation rate as a function of L_p (top), obliquity (middle), and eccentricity (bottom). Simulations with reference GCM subsurface thermal inertia are denoted with circles. Different SSI distributions at the nominal orbital geometry are shown as additional markers. The NPLD accumulation rate variations due to different SSI distributions are comparable in magnitude to those induced by orbital elements variations.

equilibrium isotopic fractionation of water upon condensation (Rossi et al., 2021) according to Merlivat and Nief (1967) relation. The isotopic composition of the condensed ice derives from two factors. First, is the isotopic enrichment of the atmosphere above the polar region, itself determined by the amount of ice condensed prior to the vapor reaching the pole (Vos et al., 2022a, 2022b). Second, is the air temperature at which the vapor condensed (Merlivat & Nief, 1967); at lower obliquity, lower polar insolation results in lower temperatures, and hence, greater fractionation. The isotopic ratio is given in δD notation, referenced to the value of the initial ice deposits. The plots show that the variations in orbital elements (with constant SSI) are reflected by significant changes in δD , as was shown in previous studies (Vos et al., 2019, 2022a, 2022b). For the various SSI distributions as above, we find that the isotopic ratio of the polar accumulation differs significantly from that of the reference SSI case. This difference in δD arises because in the southern hemisphere, the thermal inertia is 500 tiu in the reference case, significantly lower than the range obtained (1,200–2,000 tiu) for icy soils at the high filling fractions calculated in our MSIM simulations. With more heat stored in the subsurface in the high thermal inertia cases, less ice accumulates in the southern hemisphere mid-latitudes compared to the reference

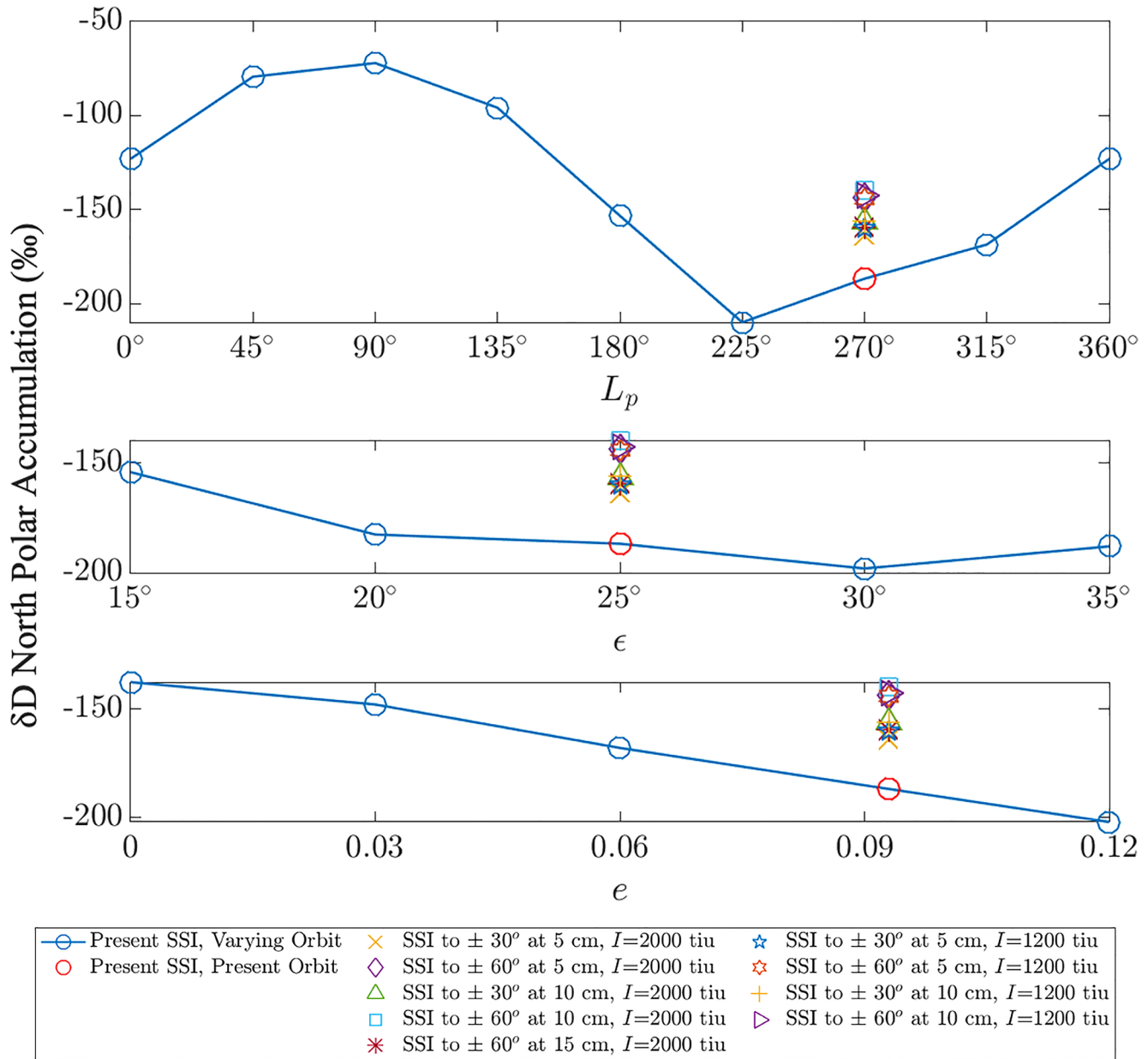


Figure 9. Isotopic anomaly of North Polar Layered Deposits ice accumulation in δD notation. Format is the same as Figure 8.

case. The remaining vapor that reaches the pole is then enriched in the heavy isotope. This is consistent with Vos et al. (2022a, 2022b), which showed that when a tropical ice source is present, the heavy isotope preferentially deposits in the equator-most latitude where surface ice condenses, leaving the atmosphere depleted in HDO when reaching the poles. We can see δD variations among the different SSI distributions, but these are smaller than the variations due to orbital parameters. We note that for other orbital configurations (not shown here), the models show the variations caused by different SSI distributions are more significant but still smaller than those due to the orbital elements (Vos et al., 2022a, 2022b).

4. Summary and Discussion

In this work, we combined two models, the Mars PCM, which simulates the atmospheric processes that act on daily and seasonal cycles, and the dynamical component of MSIM, which calculates the evolution of the SSI pore

filling on millennial timescales. The combination allows us to draw conclusions on the SSI temporal evolution and how it affects the construction of the NPLD record.

The extent of the SSI is controlled by several factors: the subsurface temperatures, the atmospheric humidity, the surface and subsurface physical properties such as thermal inertia, albedo, and the diffusion coefficient. Note, lower porosity or large rocks can strongly decrease the diffusion coefficient and, hence, decrease the flux. The atmospheric humidity is determined by the amount of insolation the surface ice reservoirs receive (Mellon & Jakosky, 1993; Schorghofer & Aharonson, 2005). We provide a parametrization of the GCM-derived annual mean water vapor column abundance that takes into account obliquity, eccentricity, L_p , and latitude.

The SSI geographic distribution, depth, and pore ice content evolve through time together with the orbital parameters, especially obliquity (Mellon & Sizemore, 2022; Schorghofer, 2007; Schorghofer & Forget, 2012). We find that the SSI extends to latitudes lower than $\pm 35^\circ$ for high obliquity. The SSI is continuously stable through orbital cycles poleward of $\pm 60^\circ$ over at least the past 10 Myr. Over obliquity cycles, the SSI fluctuates by $\sim 25^\circ$ in latitude. When the obliquity is almost constant, as in the last 0.4 Myr, there are still $\sim 10^\circ$ fluctuations in the SSI due to the precession cycle. In the latitude range where SSI has periodically accumulated and disappeared over the last ~ 3 Myr (at present between about 50° and 60° on each hemisphere), pore-filling fractions are on the order of 10%, and column-integrated ice amounts are the equivalent of decimeters of pure ice. These are the absolute abundances of ice that can be expected in these areas unless covered with a buried ice sheet.

There is evidence for present subsurface ice in equatorward latitudes (Dundas et al., 2021). These deposits may be out-of-equilibrium remnants of massive glaciers buried below thick lag layers that are slowly sublimating. In the past, there could be other surface ice distributions (Forget et al., 2006; Head et al., 2005; Levrard et al., 2004; Vos et al., 2022a, 2022b) that could change the atmospheric humidity patterns and hence change the SSI distributions. For simplicity and to reduce the number of degrees of freedom, in this work, we chose to show the SSI evolution according to present-day surface ice distribution. In past times, the departure from zonal symmetry was sometimes more significant than it is now. For example, 863 Kyr ago, when the obliquity reached 35° , SSI excursions occurred in Arcadia Planitia and near Utopia Planitia, and small concentrations of SSI can even be found in Tharsis and Elysium Mons. Our simulations for the present-day ice-table boundary show departures from zonal symmetry, mostly in the northern hemisphere. The MONS observations show similar trends as a function of longitude, though larger in amplitude (Feldman et al., 2004). The difference, which is also seen in other similar models (Schorghofer & Aharonson, 2005), may arise from incompletely modeled variations in the surface thermal structure.

About 4.5 Myr ago, the mean obliquity dropped, and the SSI retreated poleward, and over the next ~ 2 Myr, the SSI lost ~ 95 m PEL. The typical SSI flux is < 1 mm/yr PEL. In comparison, the growth rate of the NPLD at low obliquity when a tropical source is present has been estimated to be 1–6 mm/Mars year (Vos et al., 2022a, 2022b). Our simulations of the SSI pore filling are limited to the case that there are no buried glaciers in the form of massive ice. If glaciers are present, the loss from the SSI is predicted to be larger.

The SSI affects the NPLD evolution in two ways. First, it can act as an important transient source for the NPLD growth, and a minor contributor to the entire cap column. Second, the SSI also indirectly affects the polar caps' evolution by modifying the energy budget. Fluctuations in the SSI distribution change the subsurface thermal inertia, which alters the intensity of the Martian seasons and modulates the NPLD growth when a tropical source is present. The effect of the different SSI distributions on the accumulation rate is of similar magnitude to that caused by the varying orbital parameters, though its manifestation is weaker in the recorded isotopic signal. The lower sensitivity of the isotopic record to the SSI distribution could help differentiate between orbital and SSI influences on the physical stratigraphy.

These results entail that in addition to the orbital parameters and the surface ice distribution, the subsurface ice distribution must also be considered when reconstructing the NPLD profile and that several different factors control the physical and isotopic stratigraphy compared to Earth's polar isotopic profile that is affected by atmospheric temperature, distance from land and more. To decode the NPLD profile, a fully coupled model that considers multiple processes that act on different timescales must be developed.

Data Availability Statement

The code for the Mars PCM used for the simulations described in the text can be obtained at <http://svn.lmd.jussieu.fr/Planeto/trunk>, and a detailed description of it can be found in the User Manual at https://www.lmd.jussieu.fr/~lmdz/planets/mars/user_manual.pdf. The code for MSIM can be obtained in its entirety from Github at <https://github.com/nschorgh/MSIM/> and is permanently archived at Zenodo (Schörghofer, 2022). Example start files for both software can be found here (Vos, 2023). No other data set was used in this work.

Acknowledgments

We wish to thank Franck Montmessin and Margaux Vals for the helpful discussions. The authors wish to thank Bruce Jakosky and an anonymous reviewer for their helpful comments. We wish to acknowledge support from the Helen Kimmel Center for Planetary Science, the Minerva Center for Life Under Extreme Planetary Conditions 13599, and the ISF Grant 891/22. FF and EM have received funding from the European Research Council (ERC) under the European Union's Horizon 2020 research and innovation program (grant agreement No 835275, project "Mars Through Time").

References

- Aharonson, O., Vos, E., Schörghofer, N., & Forget, F. (2022). Milankovitch forcing of equilibrium ground-ice on Mars. *Proceedings of the Lunar and Planetary Science Conference*, 53.
- Bandfield, J. L., & Feldman, W. C. (2008). Martian high latitude permafrost depth and surface cover thermal inertia distributions. *Journal of Geophysical Research*, 113(E8), E08001. <https://doi.org/10.1029/2007je003007>
- Boynton, W. V., Feldman, W. C., Squyres, S. W., Prettyman, T. H., Brückner, J., Evans, L. G., et al. (2002). Distribution of hydrogen in the near surface of Mars: Evidence for subsurface ice deposits. *Science*, 297(5578), 81–85. <https://doi.org/10.1126/science.1073722>
- Byrne, S., Dundas, C. M., Kennedy, M. R., Mellon, M. T., McEwen, A. S., Cull, S. C., et al. (2009). Distribution of mid-latitude ground ice on Mars from new impact craters. *Science*, 325(5948), 1674–1676. <https://doi.org/10.1126/science.1175307>
- Diez, B., Feldman, W., Maurice, S., Gasnault, O., Prettyman, T., Mellon, M., et al. (2008). H layering in the top meter of Mars. *Icarus*, 196(2), 409–421. (Mars Polar Science IV). <https://doi.org/10.1016/j.icarus.2008.02.006>
- Dundas, C. M., Mellon, M. T., Conway, S. J., Daubar, I. J., Williams, K. E., Ojha, L., et al. (2021). Widespread exposures of extensive clean shallow ice in the midlatitudes of Mars. *Journal of Geophysical Research: Planets*, 126(3), e2020JE006617. <https://doi.org/10.1029/2020JE006617>
- Dundas, C. M., Mellon, M. T., Posiolova, L. V., Miljković, K., Collins, G. S., Tornabene, L. L., et al. (2023). A large new crater exposes the limits of water ice on Mars. *Geophysical Research Letters*, 50(2), e2022GL100747. <https://doi.org/10.1029/2022gl100747>
- Emmett, J., Murphy, J., & Kahre, M. (2020). Obliquity dependence of the formation of the Martian polar layered deposits. *Planetary and Space Science*, 193, 105047. <https://doi.org/10.1016/j.pss.2020.105047>
- Feldman, W. C., Boynton, W. V., Tokar, R. L., Prettyman, T. H., Gasnault, O., Squyres, S. W., et al. (2002). Global distribution of neutrons from Mars: Results from Mars Odyssey. *Science*, 297(5578), 75–78. <https://doi.org/10.1126/science.1073541>
- Feldman, W. C., Prettyman, T. H., Maurice, S., Plaut, J. J., Bish, D. L., Vaniman, D. T., & Tokar, R. L. (2004). Global distribution of near-surface hydrogen on Mars. *Journal of Geophysical Research*, 109(E9), E09006. <https://doi.org/10.1029/2003JE002160>
- Forget, F., Haberle, R. M., Montmessin, F., Levrard, B., & Head, J. W. (2006). Formation of glaciers on Mars by atmospheric precipitation at high obliquity. *Science*, 311(5759), 368–371. <https://doi.org/10.1126/science.1120335>
- Forget, F., Hourdin, F., Fournier, R., Hourdin, C., Talagrand, O., Collins, M., et al. (1999). Improved general circulation models of the Martian atmosphere from the surface to above 80 km. *Journal of Geophysical Research*, 104(E10), 24155–24175. <https://doi.org/10.1029/1999JE001025>
- Haberle, R. M., Forget, F., Colaprete, A., Schaeffer, J., Boynton, W. V., Kelly, N. J., & Chamberlain, M. A. (2008). The effect of ground ice on the Martian seasonal CO₂ cycle. *Planetary and Space Science*, 56(2), 251–255. <https://doi.org/10.1016/j.pss.2007.08.006>
- Head, J. W., Neukum, G., Jaumann, R., Hiesinger, H., Hauber, E., Carr, M., et al. (2005). Tropical to mid-latitude snow and ice accumulation, flow and glaciation on Mars. *Nature*, 434(7031), 346–351. <https://doi.org/10.1038/nature03359>
- Hudson, T. L., Aharonson, O., & Schörghofer, N. (2009). Laboratory experiments and models of diffusive emplacement of ground ice on Mars. *Journal of Geophysical Research*, 114(E1), E01002. <https://doi.org/10.1029/2008JE003149>
- Jakosky, B., & Carr, M. (1985). Possible precipitation of ice at low latitudes of Mars during periods of high obliquity. *Nature*, 315(6020), 559–561. <https://doi.org/10.1038/315559a0>
- Kreslavsky, M. A., & Head, J. W. (2002). Mars: Nature and evolution of young latitude-dependent water-ice-rich mantle. *Geophysical Research Letters*, 29(15), 14-1–14-4. <https://doi.org/10.1029/2002gl015392>
- Laskar, J., Levrard, B., & Mustard, J. (2002). Orbital forcing of the Martian polar layered deposits. *Nature*, 419(6905), 375–377. <https://doi.org/10.1038/nature01066>
- Laskar, J., Robutel, P., Joutel, F., Gastineau, M., Correia, A. C. M., & Levrard, B. (2004). A long-term numerical solution for the insolation quantities of the Earth. *Astronomy & Astrophysics*, 428(1), 261–285. <https://doi.org/10.1051/0004-6361:20041335>
- Leighton, R. B., & Murray, B. C. (1966). Behavior of carbon dioxide and other volatiles on Mars. *Science*, 153(3732), 136–144. <https://doi.org/10.1126/science.153.3732.136>
- Levrard, B., Forget, F., Montmessin, F., & Laskar, J. (2004). Recent ice-rich deposits formed at high latitudes on Mars by sublimation of unstable equatorial ice during low obliquity. *Nature*, 431(7012), 1072–1075. <https://doi.org/10.1038/nature03055>
- Levrard, B., Forget, F., Montmessin, F., & Laskar, J. (2007). Recent formation and evolution of northern Martian polar layered deposits as inferred from a global climate model. *Journal of Geophysical Research*, 112(E6), E06012. <https://doi.org/10.1029/2006JE002772>
- Madeleine, J.-B., Forget, F., Head, J. W., Levrard, B., Montmessin, F., & Millour, E. (2009). Amazonian northern mid-latitude glaciation on Mars: A proposed climate scenario. *Icarus*, 203(2), 390–405. <https://doi.org/10.1016/j.icarus.2009.04.037>
- Madeleine, J.-B., Forget, F., Millour, E., Montabone, L., & Wolff, M. J. (2011). Revisiting the radiative impact of dust on Mars using the LMD global climate model. *Journal of Geophysical Research*, 116(E11), E11010. <https://doi.org/10.1029/2011JE003855>
- Madeleine, J.-B., Head, J. W., Forget, F., Navarro, T., Millour, E., Spiga, A., et al. (2014). Recent ice ages on Mars: The role of radiatively active clouds and cloud microphysics. *Geophysical Research Letters*, 41(14), 4873–4879. <https://doi.org/10.1002/2014GL059861>
- Malakhov, A. V., Mitrofanov, I. G., Golovin, D. V., Litvak, M. L., Sanin, A. B., Djachkova, M. V., & Lukyanov, N. V. (2022). High resolution map of water in the Martian regolith observed by FRIEND neutron telescope onboard ExoMars TGO. *Journal of Geophysical Research: Planets*, 127(5), e2022JE007258. <https://doi.org/10.1029/2022JE007258>
- Mellon, M. T., Arvidson, R. E., Sizemore, H. G., Searls, M. L., Blaney, D. L., Cull, S., et al. (2009). Ground ice at the Phoenix landing site: Stability state and origin. *Journal of Geophysical Research*, 114(E1), E00E07. <https://doi.org/10.1029/2009JE003417>
- Mellon, M. T., Feldman, W. C., & Prettyman, T. H. (2004). The presence and stability of ground ice in the southern hemisphere of Mars. *Icarus*, 169(2), 324–340. <https://doi.org/10.1016/j.icarus.2003.10.022>
- Mellon, M. T., & Jakosky, B. M. (1993). Geographic variations in the thermal and diffusive stability of ground ice on Mars. *Journal of Geophysical Research*, 98(E2), 3345–3364. <https://doi.org/10.1029/92JE02355>

- Mellon, M. T., & Jakosky, B. M. (1995). The distribution and behavior of Martian ground ice during past and present epochs. *Journal of Geophysical Research*, *100*(E6), 11781–11799. <https://doi.org/10.1029/95je01027>
- Mellon, M. T., & Sizemore, H. G. (2022). The history of ground ice at Jezero crater mars and other past, present, and future landing sites. *Icarus*, *371*, 114667. <https://doi.org/10.1016/j.icarus.2021.114667>
- Merlivat, L., & Nief, G. (1967). Fractionnement isotopique lors des changements d'état solide-vapeur et liquide-vapeur de l'eau à des températures inférieures à 0° c. *Tellus*, *19*(1), 122–127. <https://doi.org/10.1111/j.2153-3490.1967.tb01465.x>
- Milkovich, S. M., & Head, J. (2005). North polar cap of Mars: Polar layered deposit characterization and identification of a fundamental climate signal. *Journal of Geophysical Research*, *110*(E1), E01005. <https://doi.org/10.1029/2004JE002349>
- Montmessin, F., Forget, F., Rannou, P., Cabane, M., & Haberle, R. M. (2004). Origin and role of water ice clouds in the Martian water cycle as inferred from a general circulation model. *Journal of Geophysical Research*, *109*(E10), E10004. <https://doi.org/10.1029/2004JE002284>
- Morgan, G. A., Putzig, N. E., Perry, M. R., Sizemore, H. G., Bramson, A. M., Petersen, E. L., et al. (2021). Availability of subsurface water-ice resources in the northern mid-latitudes of Mars. *Nature Astronomy*, *5*(3), 230–236. <https://doi.org/10.1038/s41550-020-01290-z>
- Piqueux, S., Buz, J., Edwards, C. S., Bandfield, J. L., Kleinböhl, A., Kass, D. M., et al. (2019). Widespread shallow water ice on Mars at high latitudes and midlatitudes. *Geophysical Research Letters*, *46*(24), 14290–14298. <https://doi.org/10.1029/2019GL083947>
- Putzig, N. E., Mellon, M. T., Kretke, K. A., & Arvidson, R. E. (2005). Global thermal inertia and surface properties of mars from the mgs mapping mission. *Icarus*, *173*(2), 325–341. <https://doi.org/10.1016/j.icarus.2004.08.017>
- Rossi, L., Vals, M., Montmessin, F., Forget, F., Millour, E., Fedorova, A., et al. (2021). The effect of the Martian 2018 global dust storm on HDO as predicted by a Mars Global Climate Model. *Geophysical Research Letters*, *48*(7), e2020GL090962. <https://doi.org/10.1029/2020GL090962>
- Schorghofer, N. (2007). Dynamics of ice ages on Mars. *Nature*, *449*(7159), 192–194. <https://doi.org/10.1038/nature06082>
- Schorghofer, N. (2008). Temperature response of Mars to Milankovitch cycles. *Geophysical Research Letters*, *35*(18), L18201. <https://doi.org/10.1029/2008GL034954>
- Schorghofer, N. (2009). Mars: Response of ice-rich permafrost to Milankovitch forcing and the origin of the polar layered deposits. In *The Lunar and Planetary Science Conference* (Vol. 40), (abstract # 1429).
- Schorghofer, N. (2010). Fast numerical method for growth and retreat of subsurface ice on mars. *Icarus*, *208*(2), 598–607. <https://doi.org/10.1016/j.icarus.2010.03.022>
- Schörghofer, N. (2022). Mars subsurface ice model (MSIM) program collection (1.2.0) [Software]. GitHub. <https://doi.org/10.5281/zenodo.6499709>
- Schorghofer, N., & Aharonson, O. (2005). Stability and exchange of subsurface ice on Mars. *Journal of Geophysical Research*, *110*(E5), E05003. <https://doi.org/10.1029/2004JE002350>
- Schorghofer, N., & Forget, F. (2012). History and anatomy of subsurface ice on Mars. *Icarus*, *220*(2), 1112–1120. <https://doi.org/10.1016/j.icarus.2012.07.003>
- Sizemore, H. G., Mellon, M. T., Searls, M. L., Lemmon, M. T., Zent, A. P., Heet, T. L., et al. (2010). In situ analysis of ice table depth variations in the vicinity of small rocks at the Phoenix landing site. *Journal of Geophysical Research*, *115*(E1), E00E09. <https://doi.org/10.1029/2009JE003414>
- Smith, D. E., Zuber, M. T., Frey, H. V., Garvin, J. B., Head, J. W., Muhleman, D. O., et al. (2001). Mars orbiter laser altimeter: Experiment summary after the first year of global mapping of Mars. *Journal of Geophysical Research*, *106*(E10), 23689–23722. <https://doi.org/10.1029/2000JE001364>
- Smith, P. H., Tamppari, L. K., Arvidson, R. E., Bass, D., Blaney, D., Boynton, W. V., et al. (2009). H₂O at the Phoenix landing site. *Science*, *325*(5936), 58–61. <https://doi.org/10.1126/science.1172339>
- Vincendon, M., Mustard, J., Forget, F., Kreslavsky, M., Spiga, A., Murchie, S., & Bibring, J.-P. (2010). Near-tropical subsurface ice on Mars. *Geophysical Research Letters*, *37*(1), L01202. <https://doi.org/10.1029/2009GL041426>
- Vos, E. (2023). Paleo-evolution of Martian subsurface ice and its role in the polar physical and isotopic layering [Dataset]. Zenodo. <https://doi.org/10.5281/zenodo.8173921>
- Vos, E., Aharonson, O., & Schorghofer, N. (2019). Dynamic and isotopic evolution of ice reservoirs on Mars. *Icarus*, *324*, 1–7. <https://doi.org/10.1016/j.icarus.2019.01.018>
- Vos, E., Aharonson, O., Schörghofer, N., Forget, F., Millour, E., Rossi, L., et al. (2022a). Climatological controls on the chemical stratigraphy of the Martian polar layer deposits. In *Seventh international workshop on the mars atmosphere: Modelling and observations* (p. 4404).
- Vos, E., Aharonson, O., Schörghofer, N., Forget, F., Millour, E., Rossi, L., et al. (2022b). Stratigraphic and isotopic evolution of the Martian polar caps from paleo-climate models. *Journal of Geophysical Research: Planets*, *127*(3), e2021JE007115. <https://doi.org/10.1029/2021JE007115>
- Zuber, M. T., Smith, D. E., Solomon, S. C., Abshire, J. B., Afzal, R. S., Aharonson, O., et al. (1998). Observations of the north polar region of Mars from the Mars orbiter laser altimeter. *Science*, *282*(5396), 2053–2060. <https://doi.org/10.1126/science.282.5396.2053>